Unconventional Charge Transport in $MgCr_2O_4$ and Implications for Battery Intercalation Hosts

Ian D. Johnson,[1,2,†] Aashutosh N. Mistry,[1,2,†] Liang Yin,[2,3] Megan Murphy,[2,4] Mark Wolfman,[1] Timothy T. Fister,[1,2] Saul H. Lapidus,[2,3] Jordi Cabana,[2,4] Venkat Srinivasan[2], and Brian J. Ingram[1,2,*]

[1] Chemical Sciences & Engineering Division, Argonne National Laboratory, Lemont, Illinois 60439, United States

[2] Joint Center for Energy Storage Research, Argonne National Laboratory, Lemont, Illinois 60439, United States

[3] X-ray Science Division, Argonne National Laboratory, Lemont, Illinois 60439, United States

[4] Department of Chemistry, University of Illinois at Chicago, Illinois 60607, United States

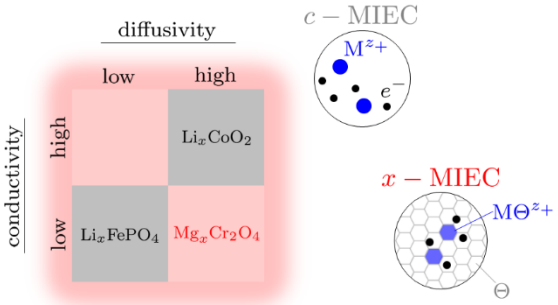

Abstract

Ion transport in solid-state cathode materials prescribes a fundamental limit to the rates batteries can operate; therefore, an accurate understanding of ion transport is a critical missing piece to enable new battery technologies, such as magnesium batteries. Based on our conventional understanding of lithium-ion materials, $MgCr_2O_4$ is a promising magnesium-ion cathode material given its reasonable computed diffusion barriers, high capacity, and high voltage against a Mg anode. Electrochemical examinations of $MgCr_2O_4$, however, reveal significant energetic limitations. Motivated by these disparate observations, herein we examine long-range ion transport by polarizing dense pellets of $MgCr_2O_4$. Our conventional understanding of ion transport in battery cathode materials, e.g., Nernst-Einstein conduction, cannot explain the measured response, since it neglects frictional interactions between mobile species and their nonideal free energies. We propose an extended theory that incorporates these interactions and reduces to the Nernst-Einstein conduction under dilute conditions. This approach better describes the measured response, and we report the first study of long-range ion transport behavior in $MgCr_2O_4$. We conclusively show that the Mg chemical diffusivity is comparable to lithium-ion electrode materials; whereas, the total conductivity is rate-limiting. Given these differences, energy storage in $MgCr_2O_4$ is limited by particle-scale voltage drops, unlike lithium-ion particles that are limited by concentration gradients. Future materials design efforts should consider the interspecies interactions described in this extended theory, particularly with respect to multivalent-ion systems, and their resultant effects on continuum transport properties.

INTRODUCTION

Future energy storage demands will require a diverse set of battery technologies that incorporate robustness of supply chain, sustainability, and low cost materials and manufacturing.[1] For these purposes, magnesium batteries are a promising opportunity to complement the state-of-the-art lithium-ion technology for our decarbonized future.[2–4] Magnesium batteries are expected to function based on the reversible redox operation of a magnesium

* Email: ingram@anl.gov

† both authors contributed equally to the work

metal anode with a suitable cathode material. Spinel oxides MgM_2O_4 (M ≡ Cr, Mn, V) are a leading cathode candidate[5] since, thermodynamically, they possess the high capacity and high voltage against the Mg anode, thereby offering the same performance advantages as lithium-ion. $MgCr_2O_4$ offers a high theoretical average voltage vs Mg^{2+}/Mg (3.5 V) and gravimetric capacity (275 mAh g^{-1}).[6] In recent years, the spinel family of materials has conclusively demonstrated reversible Mg^{2+} intercalation,[7–17] thus bolstering their promise as viable battery materials.

During electrochemical cycling of high voltage oxide cathodes, however, energetic limitations have been observed when compared against thermodynamic expectations,[10–21] limiting their utilization as a rechargeable battery technology. The fundamental sources of these limitations have not yet been fully understood, alluding to the remaining scientific challenges toward the development and commercialization of magnesium batteries in the same spirit as lithium-ion technology. For example, the electrochemical performance of a lithium-ion porous electrode[22–27] can be accurately described by a combination of bulk ion transport in the electrode active material,[28–31] electrochemical reaction (i.e., charge transfer) at the interface of active material and electrolyte,[32–34] electrolyte transport,[35–41] and conduction in carbon-binder network.[42–44] Such effects are poorly explored for the magnesium battery materials, in part due to the electrolyte stability issues[45] that obfuscate the interpretation of common electrochemical measurements characterizing relevant material properties,[11]e.g., GITT (Galvanostatic Intermittent Titration Technique) to measure chemical diffusivity in intercalation electrode materials.[34]

Herein we examine the bulk ion transport in $MgCr_2O_4$ – a candidate spinel magnesium cathode material.[6,7] The bulk ion transport sets a fundamental limit[28] on the rate at which energy can be stored and removed from the corresponding particles in porous cathodes. To maintain the charge neutrality of the material during ion intercalation, electrons enter from the external circuit. Thus, the concentration of electrons varies across the intercalation material over time in proportion to changes in ion concentration (note that concentration is a continuum property). Such simultaneous changes in ion and electron concentrations are governed by mixed ionic electronic conduction (MIEC).[47–49]

Conventionally, we assume the total conductivity for mixed conduction is a sum of conductivities of electrons and ions, $\sigma = \sigma_{\text{electron}} + \sigma_{\text{ion}}$. Past studies of Li-ion materials show that the electronic conduction is the dominant contribution such that $\sigma \approx \sigma_{\text{electron}}$. Based on this empirical understanding, bulk transport is typically believed to be limited by ion diffusion; therefore, the joint motion of ions and electrons to maintain local charge neutrality is limited by diffusion of ions, i.e., $\mathbb{D} \propto D_{\text{ion}}$. Here $\mathbb{D}$ is an ambipolar diffusivity characterizing the joint motion of ions and electrons, while D_{ion} is self-diffusivity of ions (directly related to σ_{ion}). As a result, ion diffusion barriers have been an important screening criterion for discovering new intercalation materials.[6] Based on recent computations[6] and measurement[7] of the diffusion barrier in $MgCr_2O_4$, the Mg^{2+} self diffusion is found to be reasonably facile; however, the electrochemical performance of this material has been found to be quite inferior even when the diffusion length is reduced to nanometers.[10]

Motivated by these contradictory observations, we explicitly examine the bulk long-range ion transport in $MgCr_2O_4$ to explore the nature of magnesium transport in solid-state materials. We use an electrolyte-free polarization test (thereby mitigating interfacial kinetic and decomposition effects typically complicating magnesium electrochemical studies) and show that the observed behavior does not conform to the aforementioned conventional interpretation of mixed conduction (c-MIEC). We propose an extended mixed conduction (x-MIEC) theory, of which c-MIEC is a specific case, that not only describes bulk ion transport but also makes sense of past observations that, indeed, Mg diffusion is not a limiting property in $MgCr_2O_4$.

Experimental

A series of $Mg_{1-y}Cr_{2-2y}Ti_{2y}O_4$ spinel powder and pellet samples (where 'y' was in the range $0 - 0.03$) were synthesized by two-step precipitation and annealing method as described in the Supporting Information Section S1.A. These samples are hereafter named MCO (for $MgCr_2O_4$) and MCTO(%) for the Ti-doped MCO, where (%) is the percentage of Ti in the $MgCr_2O_4$ lattice as a proportion of total transition metal content. Both the powders and the pellets formed the desired spinel phase as confirmed by synchrotron X-ray diffraction (Figure S1(a and b)). Trace MgO impurities were observed in all samples, which are commonly found in magnesium-based spinels (Figure 1(a)).[12] Both MCTO(1) and MCTO(3) contained trace $MgTi_2O_5$ or TiO_2 impurities. Simultaneous Rietveld refinement of the SXRD and neutron diffraction data confirmed Ti inclusion in the spinel lattice: the lattice parameter a increased with Ti content (Figure 1(b)). Moreover, refinement of the site occupancies confirmed the formation of the normal spinel in all samples, with negligible occupancy of Mg in 16c sites or Cr in 8a sites, which is expected to benefit bulk ion diffusion due to the reduced blocking of diffusion channels[14] (Tables S2-S4). Mg vacancies appeared to be more prevalent in the doped samples (Figure 1(b)), particularly MCTO(1), although the trends were relatively weak and the exact defect relation with Ti content cannot be confirmed. The individual particles are well defined as seen in Figure 1(c).

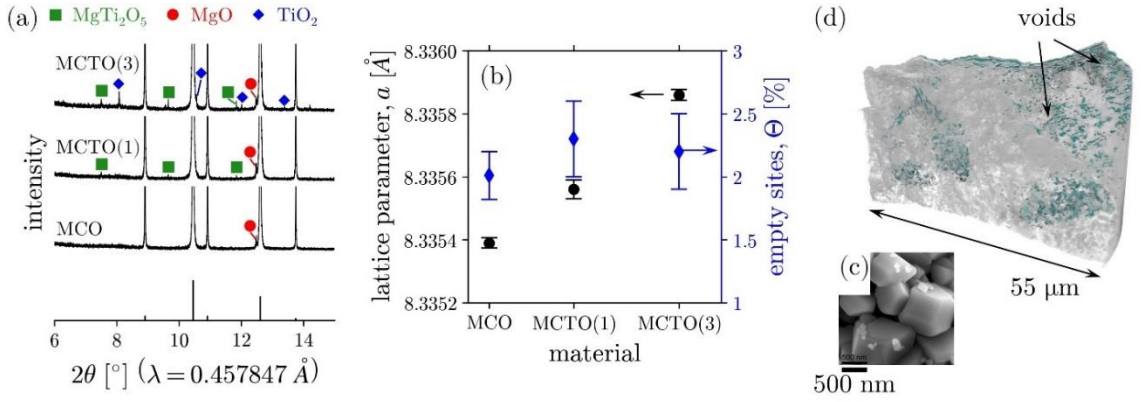

Figure 1. (a) SXRD patterns of MCO, MCTO(1), and MCTO(3) powder samples compared to a $MgCr_2O_4$ reference (ICSD Collection Code 75623)[53], with the axes limits chosen to highlight minor impurity phases. MgO, $MgTi_2O_5$, and TiO_2 impurity peaks are indicated with red circles (●), green squares (■), and blue diamonds (◆), respectively. (b) the lattice parameter *a* for the samples MCO, MTCO(1), and MTCO(3) (shown in black ●) and the concentration of Mg site vacancies shown in blue ♦. (c) an SEM image of the MCTO(1) powder. (d) 3D morphology of the MCTO(1) pellet. Voids (teal) segmented from the surrounding pellet (white) show no long-range connectivity. The black double-headed arrow shows the width of the pellet fragment used for visualization (55 µm).

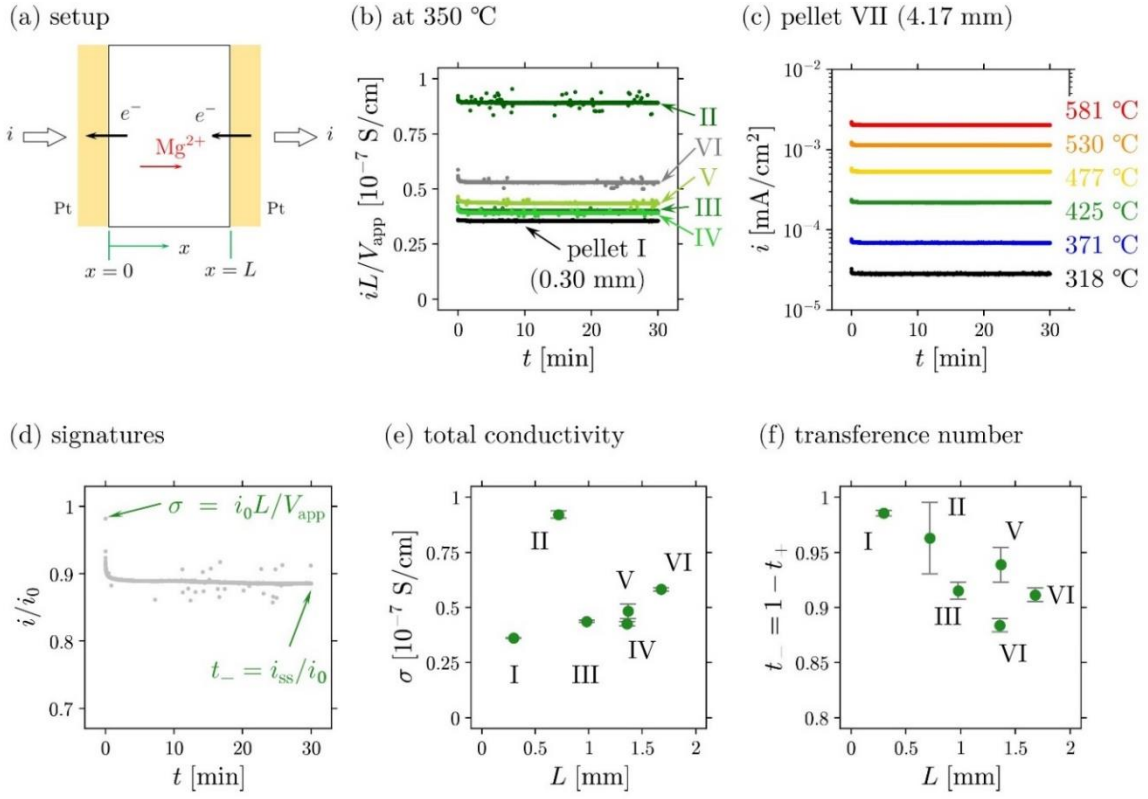

Figure 2. (a) Cell setup for transport property measurements via electrical polarization. (b) Current measurements for multiple pellets at 350°C are scaled using pellet thickness and applied voltage. (c) Variation in the current measurements for the same pellet at various temperatures. (d) A representative current measurement with conventional mixed conduction interpretation of the observed signatures. Estimated properties (e) total conductivity and (f) transference number by using the conventional mixed conduction interpretation for repeated tests performed at 350°C on six pellets with different thicknesses. Data is collected every 0.5 s in (b)-(d). Refer to Table S5 for pellet nomenclature.

The spinel phase is retained during sintering to dense pellets, as observed by SXRD, albeit with sharper diffraction peaks consistent with increased grain sizes observed in SEM (Figure S1(b-c)). Macroscopic density measurements based on pellet geometry reveal > 95% theoretical density, and X-ray Computed Tomography-based 3D reconstructions of an MCTO(1) pellet (Figure 1(d)) verifies ≤ 1.1% voids organized in a non-percolating network. Evaluation of composition variations due to phase separation was inconclusive based on EDS results; however, it should be noted that the volume fraction of second phases is < 1 % based on combined X-ray / neutron refinement. The

impurity phases are expected to be highly distributed, similar to the non-percolating network of pores. The transport measurements, therefore, of these pellets should reflect the true bulk behavior.[50] Finally, as seen in Figure S1c, the grain size is > 1 μm in sintered pellets. Impedance spectra are inconclusive in assessing relative contributions from grain core and grain boundary. We expect the conduction measurements, however, are dominated by bulk grain core since we do not observe a change in the Arrhenius behavior as a function of temperature[51] and micron sized grains[52].

We selected MCTO(1) for transport measurements since it possesses the highest concentration of Mg vacancies with minimal impurities and measured the temperature- and thickness-dependent polarization behavior of MCTO(1) pellets using an electrolyte-free arrangement as shown in Figure 2(a) (refer to Table S5 for specifications of the polarization tests). This configuration is common across many fields, e.g., electroceramics, and the measured behavior has been historically explained using c-MIEC theory[54–64] (dating back to classical works by Hebb[47], Wagner[48], and Yokota[49]). We note that Stefan et al.[51,65] have measured conductivity of porous pellets of numerous Mg-based spinel compositions without exploring mixed conduction properties. Pt electrodes are sputtered on either surface of the pellet (refer to Supporting Information Section S1.C for further details) to ensure uniform current density across the pellet cross-section when current passes through the pellet. During polarization at a constant voltage, the observed current decays over time (Figure 2(b)-(d)) due to the blocking nature of the Pt electrodes and formation of concentration gradients of charged species. As Pt has high electrical conductivity, it is not expected to contribute to the observed responses in Figure 2(b)-(d). It should be noted that data were collected every 0.5 s and the apparent outlier data points for a given data set in Figure 2(b)-(d) represent < 1% of the total collected.

If we interpret these measurements using c-MIEC theory,[47–49,57] we note inconsistency while inferring diffusivity from conductivity estimates. According to this theory, the two endpoints, i_0, and i_{ss} can be used to quantify σ (Figure 2(e)) and t_- (Figure 2(f)). As per c-MIEC, the total conductivity, σ, relates to self-diffusion of both the charged species (also known as the Nernst-Einstein relation; Eq. S16 in Supporting Information Section S2):

$$\sigma = \frac{2F^2}{RT} c(2D_+ + D_-) = \frac{4F^2}{3RT} c \frac{\mathbb{D}}{t_-(1-t_-)} \quad [1]$$

The second equality in Eq. [1] is by the definition of ambipolar diffusivity, $\mathbb{D}$ (Eq. S14). Once σ and t_- are measured as shown in Figure 2(d), Eq. [1] (i.e., the c-MIEC theory) can be used to estimate $\mathbb{D}$.

$$\mathbb{D} = \sigma \frac{3RT}{4F^2 c} t_-(1-t_-) \quad [2]$$

The ambipolar diffusion, $\mathbb{D}$, is the joint motion of Mg^{2+} cations and e^- such that local charge neutrality is ensured. Based on σ from Figure 2(e), t_- from Figure 2(f), and $c = 23$ M defined by material density, Eq. [2] gives $\mathbb{D} \sim 4 \times 10^{-14}$ $cm^2\ s^{-1}$ for the six pellets of $MgCr_2O_4$ (I to VI in Table S5) polarized at the same temperature (350 °C). In contrast, the time scale for current decay in Figure 2(d) is ~10 min, which suggests a diffusivity, $\mathbb{D} = L^2/t \sim 2 \times 10^{-5}$ $cm^2\ s^{-1}$.

This stark mismatch in the two diffusion coefficients indicates that the mixed conduction behavior in this material differs from c-MIEC expectations. In the subsequent discussion, we propose an extended mixed conduction theory (x-MIEC) to explain the observed response.

THEORY

Consider a host material, Θ, intercalating a cation, M^{z+}. Its fully deintercalated state is Θ, and fully intercalated state is MΘ. For every cation intercalating in this host, n electrons enter through the external circuit to maintain global charge neutrality. Thus, transport in an intercalation host can be conceptualized in terms of three mobile species: $M\Theta^{z+}$ (cation occupied host), e^- (mobile electrons) and Θ (unoccupied host).[66,67] This is schematically shown in Figure 3. Each of the species influence the microscopic motion of the other. Such interactions are captured using three distinct Stefan-Maxwell diffusivities. A Stefan-Maxwell diffusivity, $\mathfrak{D}_{ij}$, describes relative motions of

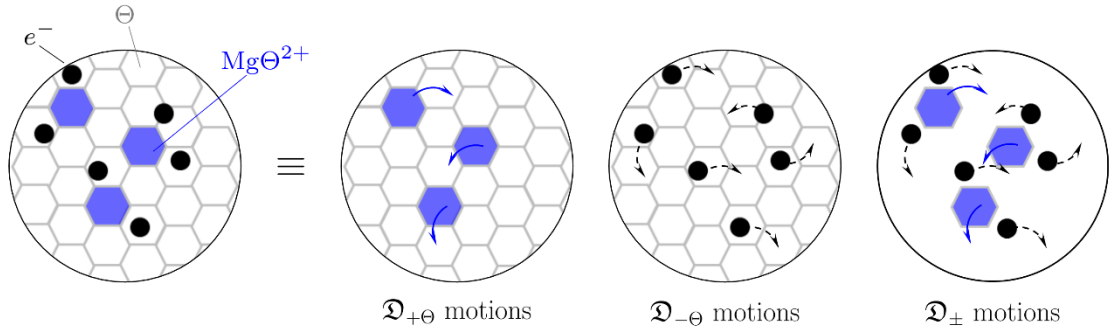

Figure 3. A schematic representation of microscopic species and their relative motions in an Mg-intercalation host. There are three species: electrons, e^-, unoccupied host, Θ, and cation occupied host, $Mg\Theta^{2+}$. The relative motion of two species is accounted for using the corresponding Stefan-Maxwell diffusivity. Accordingly, the species transport in an intercalation host is described using three Stefan-Maxwell diffusivities: $\mathfrak{D}_{+\Theta}$, $\mathfrak{D}_{-\Theta}$ and $\mathfrak{D}_{\pm}$

species i and j. $\mathfrak{D}_{ij}$ implicitly accounts for correlated and uncorrelated motions of these species averaged over a large number of i and j 'particles' to represent the continuum behavior (here 'particles' implies individual entities like electrons, cations, host unit cells, etc.). We, thus, use the Stefan-Maxwell equations to describe the transport behavior of these species:

$$-\frac{c_+c_T}{RT}\nabla\mu_+ = \frac{(c^{\max}-c)N_+ - c_+N_\Theta}{\mathfrak{D}_{+\Theta}} + \frac{c_-N_+ - c_+N_-}{\mathfrak{D}_\pm} \quad [3]$$

$$-\frac{c_-c_T}{RT}\nabla\mu_- = \frac{(c^{\max}-c)N_- - c_-N_\Theta}{\mathfrak{D}_{-\Theta}} + \frac{c_+N_- - c_-N_+}{\mathfrak{D}_\pm} \quad [4]$$

where N's are corresponding species fluxes, and $\mathfrak{D}_{ij}$'s are Stefan-Maxwell diffusivities. Here μ_+ and μ_- are electrochemical potentials of $M\Theta^{z+}$ and e^-, respectively. The maximum concentration of cations, $c^{\max}$, is a material property. At a given degree of intercalation, $c_+ = \nu_+c, c_- = \nu_-c$ and $c_\Theta = c^{\max} - c$. Here ν_+ and ν_- are stoichiometric coefficients. Note that any of the species can be present in high concentrations depending on the degree of intercalation. The third Stefan-Maxwell relation for Θ is not independent of Eqs. [3] and [4] due to the Gibbs-Duhem relation:

$$c_+\nabla\mu_+ + c_-\nabla\mu_- + (c^{\max}-c)\nabla\mu_\Theta = c\nabla\mu_{M\Theta} + (c^{\max}-c)\nabla\mu_\Theta = 0 \quad [5]$$

Here $c_+\nabla\mu_+ + c_-\nabla\mu_- = c\nabla\mu_{M\Theta}$.

c-MIEC theory[47–49] does not account for the cation – electron interactions in Eqs. [3], [4] (mathematically, $\mathfrak{D}_\pm \to \infty$) and assumes that the unoccupied host does not move ($N_\Theta = 0$) in response to an applied voltage.

It is easy to show that for $M\Theta^{z+}$ and e^- as positively and negatively charged species $\nu_+ = 1$ and $\nu_- = n$, and the corresponding charges are $z_+ = n$ and $z_- = -1$. The statement of local charge neutrality can be written in terms of concentrations or stoichiometries as

$$z_+c_+ + z_-c_- = 0 = z_+\nu_+ + z_-\nu_- \quad [6]$$

By definition, the current density is associated with the flux of charged species as,

$$\frac{i}{F} = z_+N_+ + z_-N_- \quad [7]$$

Rearranging Eqs. [3],[4] and [7],

$$N_- = -\frac{\nu_-}{RT}\frac{1}{\left(\frac{\nu_+}{\mathfrak{D}_{+\Theta}}+\frac{\nu_-}{\mathfrak{D}_{-\Theta}}\right)}\frac{cc_T}{(c^{\max}-c)}\nabla\mu_{M\Theta} + \frac{\frac{\nu_+}{\mathfrak{D}_{+\Theta}}}{\left(\frac{\nu_+}{\mathfrak{D}_{+\Theta}}+\frac{\nu_-}{\mathfrak{D}_{-\Theta}}\right)}\frac{i}{z_-F} + \nu_-cv_\Theta \quad [8]$$

$$\therefore N_- = -\nu_-\mathbb{D}\nabla c + \left(1-t_+^\Theta\right)\frac{i}{z_-F} + \nu_-cv_\Theta \quad [9]$$

where the properties are grouped to define the ambipolar diffusivity, $\mathbb{D}$, and the cation transference number, t_+^Θ, as

$$\mathbb{D} = \frac{\nu}{\left(\frac{\nu_+}{\mathfrak{D}_{+\Theta}}+\frac{\nu_-}{\mathfrak{D}_{-\Theta}}\right)}\frac{c_T}{(c^{\max}-c)}\left(1+\frac{\partial\ln f_{M\Theta}}{\partial\ln c}\right) \quad [10]$$

$$t_+^\Theta = \frac{\frac{\nu_-}{\mathfrak{D}_{-\Theta}}}{\left(\frac{\nu_+}{\mathfrak{D}_{+\Theta}}+\frac{\nu_-}{\mathfrak{D}_{-\Theta}}\right)} \quad [11]$$

where $(1+\partial\ln f_{M\Theta}/\partial\ln c)$ is the thermodynamic factor described in Section S3. For battery materials, the thermodynamic factor directly relates to the open circuit potential.

The corresponding expression for the cation flux is,

$$N_+ = -\nu_+\mathbb{D}\nabla c + t_+^\Theta\frac{i}{z_+F} + \nu_+cv_\Theta \quad [12]$$

and, the current density expression is

$$\frac{i}{F}\left\{\frac{(c^{\max}-c)\left(1-t_+^\Theta\right)}{z_-\mathfrak{D}_{-\Theta}} + \frac{\nu_+c}{z_-\mathfrak{D}_\pm}\right\} = -\frac{c_-c_T}{RT}\nabla\mu_- + \frac{\nu_-}{\mathfrak{D}_{-\Theta}}(c^{\max}-c)\mathbb{D}\nabla c \quad [13]$$

It is crucial to accurately define the electrochemical potential of e^- in the host, μ_-. Since the host material is in contact with the external circuit, the equilibrium statement can be written as

$$\mu_{e^-_{\text{host}}} = \mu_{e^-_{(s)}} = z_-F\phi \quad [14]$$

Here e^-_{host} and $e^-_{(s)}$ are respectively the mobile electrons in host and adjoining Pt contact. Note that we do not have to explicitly account for the concentration dependence of electrons in the externally measured potential, ϕ. The electrochemical potential of the intercalated cations, $M\Theta^{z+}$, is related to ϕ and local concentration since

$$\frac{1}{n}\mu_{M\Theta} = \frac{1}{n}\mu_{M\Theta^{z+}} + \mu_{e^-} = \frac{1}{n}\mu_+ + \mu_- \quad [15]$$

Instead, if the potential were measured using an electrode reversible to $M\Theta^{z+}$, ϕ relates to $\mu_{M\Theta^{z+}}$, and then μ_{e^-} will depend on ϕ and concentration. Using Eqs. [14], [10] and [11] in the current density expression (Eq. [13]),

$$i = -\sigma\left(\nabla\phi + t_+^\Theta\frac{\nu}{\nu_+z_+}\frac{RT}{F}\left(1+\frac{\partial\log f_{M\Theta}}{\partial\log c}\right)\nabla\ln c\right) \quad [16]$$

where total conductivity, σ, is an additional *measurable* property,

$$\sigma = z_+^2\nu_+\frac{F^2}{RT}\frac{c_T}{\left\{\frac{\nu_-}{\mathfrak{D}_\pm} + \frac{(c^{\max}-c)t_+^\Theta}{c\mathfrak{D}_{+\Theta}}\right\}} \quad [17]$$

Note that the (continuum) flux of the unoccupied host, N_Θ, is related to its concentration and velocity as

$$N_\Theta = c_\Theta v_\Theta = (c^{\max}-c)v_\Theta \quad [18]$$

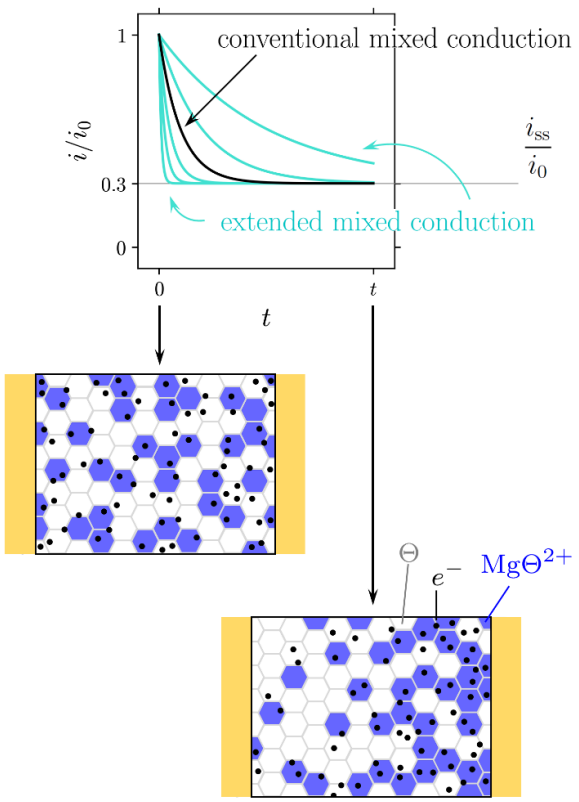

Figure 4. Comparing conventional and extended mixed ionic electronic conduction behaviors. For a given initial current density, i_0, and the ratio of current densities at the steady state, i_{ss}/i_0, the conventional mixed conduction is uniquely defined. Any departure from this behavior is representative of the extended mixed conduction response. Schematics of microscopic species arrangement are also shown.

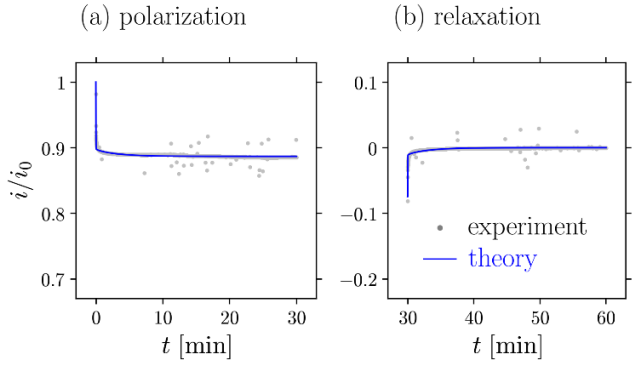

Figure 5. x-MIEC analysis of the transient processes during (a) polarization after external application of a voltage at t = 0 min and (b) relaxation when the voltage is removed at t = 30 min. Current data (grey circles) are collected every 0.5 s and the x-MIEC fit (blue line) is based on an error minimization algorithm (see Section S4). For a given experimental set, this error is a function of the material properties, $R_i, C_i, \sigma, \mathcal{D}$ and $\mathbb{Ne}$.

The Stefan-Maxwell expressions (Eqs. [3] and [4]) involve three diffusivities, $\mathfrak{D}_{+\Theta}, \mathfrak{D}_{-\Theta}, \mathfrak{D}_{\pm}$, and equivalently the constitutive relations (Eqs. [9], [12], [16] and [18]) involve three independent transport properties, $\mathbb{D}, t_+^{\Theta}$, and σ. Additionally, the thermodynamic factor accounts for the nonideal energies of the intercalation host (related to the deviation from the Nernst potential of the open circuit potential).

The polarization behavior of the test configuration shown in Figure 2(a) can be described using the x-MIEC constitutive relations developed here (Eqs. [9], [12], [17] and [18]). The specific steps are shown in Section S4. Thus, Eqs. [S50], [S54]-[S58] jointly represent the polarization of the pellets and are equally valid for potentiostatic and galvanostatic responses. Five unique properties characterize the polarization response: $R_i, C_i, \sigma, \mathcal{D}$ and $\mathbb{Ne}$, where R_i is interfacial resistance for electron transfer across Pt/pellet interface, C_i is capacitance at this interface, $\mathcal{D}$ is chemical diffusivity and $\mathbb{Ne}$ is Newman number.

$$\mathcal{D} = \mathbb{D}\left(1 - \frac{c}{c^{\max}}\right) \qquad [19]$$

$$\mathbb{Ne} = \sigma \frac{3RT}{4F^2}\left(t_+^{\Theta}\right)^2 \left(1 + \frac{\partial \ln f_{M\Theta}}{\partial \ln c}\right)\frac{1}{c\mathbb{D}} \qquad [20]$$

The Newman number is defined here for measurements using electron selective probe electrodes (alternatively, $\mathbb{Ne}$, as defined by Balsara and Newman,[68] is for cation-selective probe electrodes). The definition of $\mathbb{Ne}$ is more significant than just a dimensionless descriptor and is related to the measurable quantities of steady-state and initial current, if the interfacial effects were negligible, such that

$$\frac{i_{ss}}{i_0} = \frac{1}{1 + \mathbb{Ne}} \qquad [21]$$

Recall that in the conventional mixed conduction theory, $i_{ss}/i_0 = t_-$ (Figure 2(d); section S2.B). Hence, as shown in Figure 4, c-MIEC behavior is uniquely defined given the initial current density, i_0 (prescribing σ), and the ratio at the steady-state, i_{ss}/i_0 (prescribing t_-). Alternatively, multiple different x-MIEC responses can manifest even when these two values are fixed. Mathematically, this difference is due to having only two independent properties in c-MIEC versus four $\left(\sigma, t_+^{\Theta}, \mathbb{D}, \left(1 + \frac{\partial \ln f_{M\Theta}}{\partial \ln c}\right)\right)$ in x-MIEC (refer to Figure S2). It should be emphasized that [17] reduces to the Nernst-Einstein relationship (Eq [1]) as $c \to 0$, i.e., as the concentration of $Mg\Theta^{2+} \to 0$; the corresponding expressions are provided in Table 1. The specific concentration, c, below which x-MIEC simplifies to the c-MIEC interpretation is strongly dependent on the material being examined.

RESULTS AND DISCUSSION

As discussed in Figure 2(d), the c-MIEC analysis of the current profiles relies on the initial and steady-state currents. Instead, x-MIEC behavior, as proposed here, is composed of multiple processes, each of which is dominant over different time intervals (Figure 5(a-b)): interfacial resistance, R_i, interfacial capacitance, C_i, and total

conductivity, σ, are the dominant contributions at short timescales, whereas chemical diffusivity, $\mathcal{D}$, and Newman number, $\mathbb{Ne}$ influence longer timescales. Hence, we estimate these properties by analyzing the full polarization and relaxation step as shown in Figure 5 and Figure S3. Figure S6 shows that unique values of these five properties give the least difference between the theoretically predicted behavior and the measured response. Such a uniqueness is guaranteed as each of the properties exhibit distinct signatures on the polarization response (Figure S3). Figure 5 compares the modeled response using the estimated properties against measurements. Thus, the estimated properties capture the underlying variability in the experimental data. As mentioned in Table S5, each pellet is tested multiple times and each such experimental set is analyzed to obtain corresponding property estimates. Thus, the multiple property groups for each pellet tested at a given temperature also characterize the random error in experiments. The pellet resistance versus time evolutions are comparable regardless of applied polarization (0.25, 0.5, 0.75 and 1 V) suggesting a linear response to polarization. Furthermore, X-ray diffraction analysis of pellets showed no discernable changes before and after polarization. This is further corroborated by the reversible and repeatable nature of the polarization experiments, showing consistent responses with subsequent application of potentiostatic holds.

Table 1. Comparing the expressions for measurable properties between c-MIEC and x-MIEC. D identifies self-diffusivities, while $\mathfrak{D}_{ij}$'s are Stefan-Maxwell diffusivities.

	c-MIEC	**x-MIEC**
total conductivity	$\sigma = 2\frac{F^2}{RT}c(2D_+ + D_-)$	$\sigma = 2\frac{F^2}{RT}c_T\left\{\frac{2}{\mathfrak{D}_\pm} + \frac{(c^{\max}-c)t_\pm^\Theta}{c\mathfrak{D}_{+\Theta}}\right\}^{-1}$
cation transference number	$t_+ = \frac{2D_+}{2D_+ + D_-}$	$t_+^\Theta = \frac{2\mathfrak{D}_{+\Theta}}{2\mathfrak{D}_{+\Theta} + \mathfrak{D}_{-\Theta}}$
ambipolar diffusivity	$\mathbb{D} = \frac{3D_+D_-}{2D_+ + D_-}$	$\mathbb{D} = \frac{3\mathfrak{D}_{+\Theta}\mathfrak{D}_{-\Theta}}{2\mathfrak{D}_{+\Theta} + \mathfrak{D}_{-\Theta}} \cdot \frac{c_T}{(c^{\max}-c)}\left(1 + \frac{\partial \ln f_{M\Theta}}{\partial \ln c}\right)$
total concentration	–	$c_T = c^{\max} + c$
Newman number	–	$\mathbb{Ne} = \sigma\frac{3RT}{4F^2}\left(t_+^\Theta\right)^2\left(1 + \frac{\partial \ln f_{M\Theta}}{\partial \ln c}\right)\frac{1}{c\mathbb{D}}$
current ratio	$\frac{i_{ss}}{i_0} = t_- = (1 - t_+)$	$\frac{i_{ss}}{i_0} = \frac{1}{1 + \mathbb{Ne}}$

Figure 6 plots bulk transport properties, $\sigma, \mathcal{D}$ and $\mathbb{Ne}$, following the x-MIEC interpretation of the experimental observation. The analysis for the same six pellets as Figure 2(b) is shown here. Since all materials are identical and the interfaces are prepared with nominally identical procedures (sputtered Pt), ideally these properties should be independent of the pellet thickness. The contributions of the bulk properties, relative to interfacial properties, scale with pellet thickness, and the bulk signatures in Figure 6 become less pronounced for very thin pellets. The diminishing signatures for thinner pellets set a practical lower bound on the pellet thickness necessary to characterize mixed conduction behavior. On the other hand, the upper bound on the pellet thickness is set by the dimensions of the die within the hot press used to make these pellets. We explore pellet thicknesses in between these two bounds. Thus, Figure 6 characterizes the variations in the measured properties at different thicknesses. Note that two of these pellets, IV and V, have comparable thicknesses (1.36 and 1.37 mm, respectively), and the corresponding estimates characterize the sample-to-sample variability. Thus, the estimated property variations in Figure 6 are composed of two effects: sample-to-sample variability and the more dominant role of interfacial properties for thinner pellets. Such variations are intrinsically present when analyzing material behavior composed of interfacial and bulk effects. For each pellet, the error bars represent the standard deviation in the estimated property. As shown in Figure S3, the analysis scheme identifies five properties for every experimental set, and the two corresponding interfacial properties are reported in Figure S7.

Note that the chemical diffusion, $\mathcal{D}$, in Figure 6(b) is comparable to that inferred based on the current decay timescale in Figure 2(d), thus offering a consistent view of charge transport. While the current decay timescale in Figure 2(d) provides diffusivity without invoking the x-MIEC theory, the corresponding physical interpretation is unclear. As revealed by Eqs. [10] and [19], the observed diffusion represents a joint motion of all three mobile species and thermodynamic nonidealities. Thus, x-MIEC is instrumental in interpreting the measurements for this material and linking them to ion transport behavior. Figure 7 presents the temperature dependence of estimated bulk properties for two pellets with different thicknesses (VII and VIII in Table S5). Notice that any differences between estimated properties for the two pellets at each

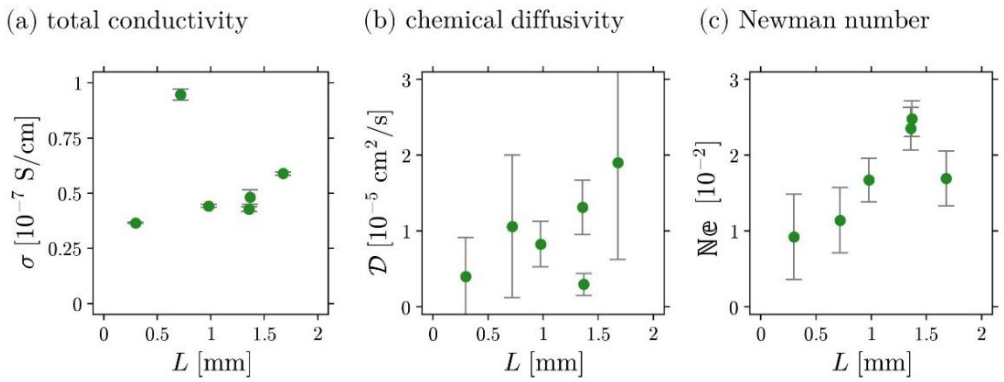

Figure 6. Bulk transport properties for multiple pellets at 350°C (I to VI in Table S5). (a) Total conductivity, σ. (b) Chemical diffusivity, $\mathcal{D}$. (c) Newman number, $\mathbb{N}\mathbb{e}$. (a) – (c) plot mean values along with standard deviation as corresponding error bars for each pellet. Corresponding interfacial properties are reported in Figure S7.

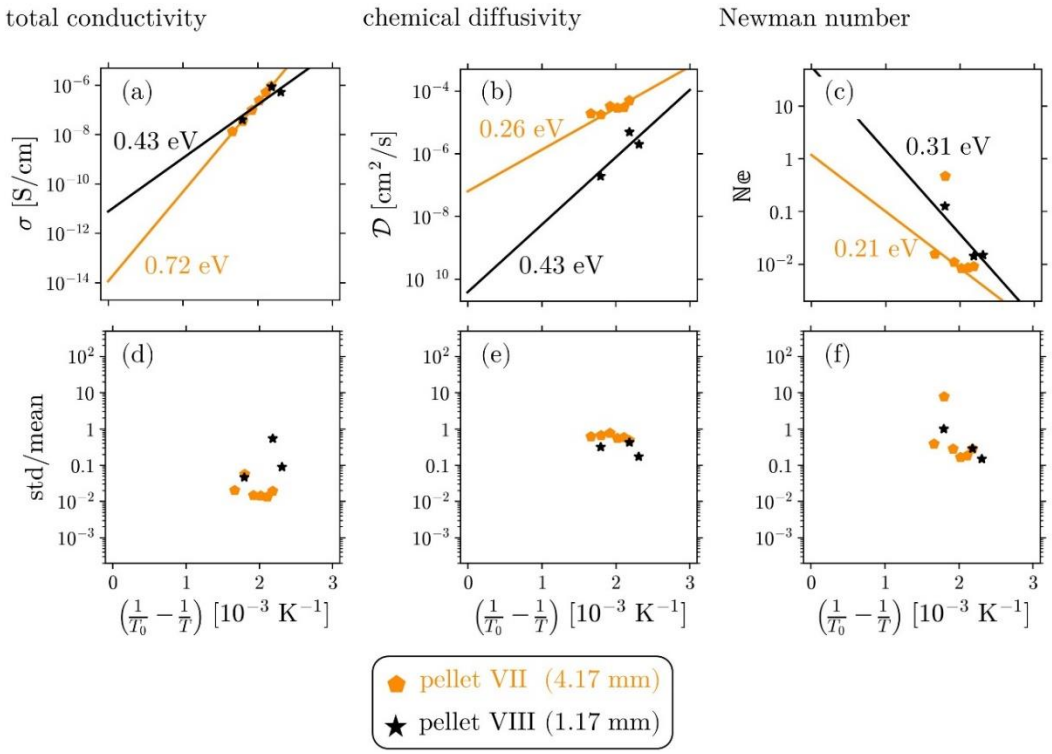

Figure 7. Temperature dependence of estimated bulk properties for two pellets of the same materials. (a), (d) Total conductivity, σ. (b), (e) Chemical diffusivity, $\mathcal{D}$. (c), (f) Newman number, $\mathbb{N}\mathbb{e}$. (a) – (c) show the mean estimates, while (d) – (f) plot corresponding standard deviations scaled to mean. The activation energies have been quantified by fitting Arrhenius dependence through all estimates. $T_0 = 298$ K. The differences in the estimates between the two pellets are predominantly related to the differences in their thicknesses. Corresponding estimated interfacial properties are shown in Figure S8.

temperature result from the variabilities discussed in Figure 6. By comparing variations of each property in Figure 7 with Figure 6, it is clear that the temperature dependence of each property is prominent.

As expected, both total conductivity, σ, (Figure 7(a)) and chemical diffusivity, $\mathcal{D}$, (Figure 7(b)) exhibit Arrhenius dependences. The Arrhenius behavior is consistent with prior measurements of conductivity within $MgCr_2O_4$ by Stefan et al,[51,65] although their analysis did not specifically examine diffusive effects. The activation energies for the two pellets within our study are not identical. This is in part related to more dominant interfacial behavior for the thinner pellet. For each pellet, the useful temperature range is limited by very large resistances at lower temperatures and very small resistances at higher temperatures. Therefore, our experiments were conducted entirely within the temperature window (350-600 °C) where transport signatures could be robustly characterized and allowed us to extrapolate to room temperature for direct comparison with known Li-ion battery cathodes.

As per Figure 7(c), $\mathbb{N}\mathbb{e}$ decreases with temperature. Since the concentration overpotential is related to $\mathbb{N}\mathbb{e}$, Figure 7(c)

suggests that the chemical diffusion signature becomes less pronounced. More importantly, in the limit of low temperature, chemical diffusion becomes increasingly relevant. As per Eq. [20], such behavior of $\mathbb{Ne}$ leads to $i_{ss}/i_0 \to 1$ at higher temperatures and $i_{ss}/i_0 \to 0$ at lower temperatures. If these limits were interpreted using c-MIEC, one may mistakenly conclude that the conduction is electronically dominated at higher temperatures ($i_{ss}/i_0 \to 1$) and ionically dominated at lower temperatures ($i_{ss}/i_0 \to 0$).

Figure 7(d)-(f) report the variability in the estimated bulk properties based on repeated testing at each temperature. These variations reflect the reproducibility of measurements at each temperature and underscore the importance of meticulous testing. The corresponding estimates of the interfacial properties, R_i and C_i, are plotted in Figure S8.Figure 8 compares the mixed conduction properties of $MgCr_2O_4$ against well-characterized known Li-ion materials at room temperature (25°C) by extrapolating the Arrhenius relationships of the chemical diffusivity ($\mathcal{D}$) and total conductivity (σ) behavior in Figure 7. We find that the chemical diffusivity of $MgCr_2O_4$ is comparable to most Li-ion materials, but its conductivity is considerably smaller. This observation is in stark contrast to conventional expectations, where both diffusivity and conductivity increase proportionately (as observed for Li-ion materials in Figure 8). The expectation of proportionately linked conductivity and diffusivity is a feature of c-MIEC behavior (Eq. [2]). $MgCr_2O_4$ deviates significantly from the relationship followed by Li-ion cathodes and its polarization behavior, e.g., Figure 2(d) cannot be analyzed using c-MIEC. The newly proposed x-MIEC captures the observed charge transport in $MgCr_2O_4$ as well as the usual c-MIEC as a special case. The significant difference between Li-ion electrode materials and $MgCr_2O_4$ at room temperature implies that the particle-scale intercalation response of $MgCr_2O_4$ is dictated by conduction (voltage drop); in contrast, most Li-ion electrode particles are limited by diffusion (concentration gradients).[23–25,33,69–71] These observations of charge transport in $MgCr_2O_4$ suggests that the traditional thinking of Mg transport in terms of cation-lattice interactions, which assigns sluggish cation self-diffusion as the limiting mechanism for Mg intercalation, is not always valid.

In comparison to the c-MIEC, the most interesting characteristic of x-MIEC is that the chemical diffusivity and conductivity – both material properties defining different aspects of charge transport – are not always proportionately related. Within our study, x-MIEC behavior was evident in the polarization response of $MgCr_2O_4$, with a diffusion signature that decayed much faster than expectations from c-MIEC theory. There are two key effects governing this relationship between chemical diffusivity and total conductivity: the intrinsic relative motion of charged species, as quantified by $\mathfrak{D}_\pm$, which only contributes to conductivity, whereas the chemical diffusivity is dependent on nonideal energies of mobile species via the thermodynamic factor (refer to Table 1). The specific concentration, c, below which x-MIEC simplifies to the c-MIEC Nernst-Einstein interpretation is dependent on the material being examined.

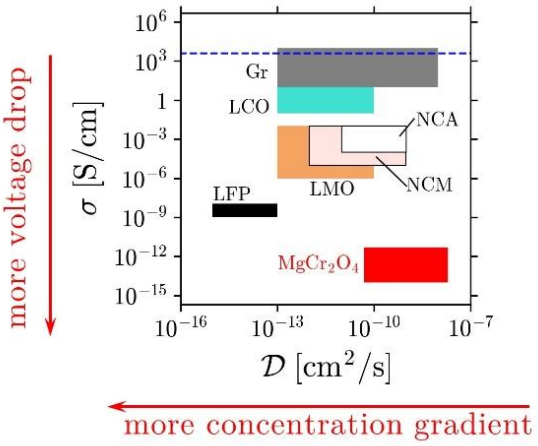

Figure 8. Comparing the estimated transport properties in $MgCr_2O_4$ against Li-ion properties from literature. Typically, the carbon-binder phase is added to the porous electrode to improve long-range electron conduction. The bulk conductivity of the carbon-binder phase[72] is also shown for comparison as a dashed horizontal line. All properties are at room temperature, 25°C (see Table S5).[28–31,71,73–75] The $MgCr_2O_4$ properties are obtained by extrapolating the Arrhenius lines in Figure 7(a) and (b). Gr ≡ graphite (Li_xC_6). LCO ≡ Li_xCoO_2. NCA ≡ $Li_xNi_{0.8}Co_{0.15}Al_{0.05}O_2$. NCM ≡ $Li_xNi_{0.33}Co_{0.33}Mn_{0.33}O_2$. LMO ≡ $Li_xMn_2O_4$. LFP ≡ Li_xFePO_4.

Previous studies probing cation self-diffusion offered a partial picture of charge transport limitations for $MgCr_2O_4$ but provided key guidance for materials development. In light of the present findings, refinement of the existing computational screening paradigm for battery intercalation hosts to account for Stefan-Maxwell diffusivities should be considered. At present, however, a consistent approach to predicting Stefan-Maxwell diffusivities from atomistic calculations is challenging. Given these nuances, a pragmatic approach for discovering new multivalent cation cathodes should be complementing high-throughput self-diffusion screening with long-range charge transport measurements to underpin a more complete picture of mixed conduction mechanisms.

CONCLUSIONS

Magnesium batteries are promising chemistry to expand the existing battery portfolio to meet future energy storage demands, where $MgCr_2O_4$ is a candidate high-voltage cathode material. However, when operated electrochemically, the measured response of $MgCr_2O_4$ falls short of theoretical expectations. A likely limitation is the transport of intercalated Mg^{2+} ions in this material, and the present study investigates long-range transport behavior.

To explicitly probe the ion transport within the bulk material, we employ an electrolyte-free configuration that electrically polarizes dense $MgCr_2O_4$ pellets. Traditionally, such measurements are interpreted using the conventional mixed ionic electronic conduction (c-MIEC) theory to estimate representative transport properties such as

Nernst-Einstein conductivity. Unexpectedly, the measured behavior of $MgCr_2O_4$ does not conform to c-MIEC theory; therefore, we propose an extended mixed conduction (x-MIEC) theory that resolves this discrepancy. While c-MIEC assumes that the charge carriers are present in dilute concentrations and exhibits thermodynamically ideal energies, x-MIEC relaxes these assumptions by accounting for interspecies interactions and nonideal energies.

We compared Arrhenius extrapolations of $MgCr_2O_4$ x-MIEC transport properties (total conductivity, chemical diffusivity, Newman number) with known Li-ion materials at room temperature. Based on this comparison, Mg chemical diffusion is not the limiting mechanism for the ion transport in $MgCr_2O_4$; rather, the total conductivity is rate-limiting. On the other hand, most Li-ion materials are limited by diffusion. Consequently, for ion transport within $MgCr_2O_4$ to compete with Li-ion materials, strategies for improving conductivity should be pursued instead of maximizing diffusivity. Indeed, future work will focus on extension of this x-MIEC analysis to other spinel compositions (such as $MgCrMnO_4$ and MgV_2O_4) which are anticipated to possess higher conductivity than $MgCr_2O_4$. Overall, both voltage drop and concentration gradient effects should be considered when designing active particles for porous Mg battery electrodes.

Given we observe a deviation from expected c-MIEC in stoichiometric $MgCr_2O_4$, and its intended application stores energy by varying Mg content, future work will investigate mixed conduction at corresponding concentrations. Moreover, it is imperative to examine whether this peculiar mixed conduction behavior is a characteristic of Mg^{2+} transport in a wider range of cathode materials, or can even be found in a broader range of mixed conductors for other applications, e.g. new Li-ion electrode materials, solid-oxide fuel cell cathodes, and electrocatalysts. We note that x-MIEC describes c-MIEC behavior as a limiting case, and therefore, x-MIEC promises broad utility to describe charge transport in MIECs. To facilitate materials design of mixed conductors, we need to underpin the defect chemistry origins of x-MIEC theory by systematically connecting microscopic and continuum interpretations of transport. Namely, for a given solid-state material, there is a need to identify the (degree of) intercalation window where c-MIEC breaks down.

There are similarities between ion transport in liquid and polymer electrolytes, as described by Newman's concentrated solution theory,[76–78] and mixed conduction in solids as identified here using x-MIEC. Specifically, the counter ion and neutral solvent in electrolytes appear to exhibit philosophical similarities to electrons (or holes) and unoccupied hosts in solids, respectively. This alludes to a possible unified understanding of charge transport across different media.

ASSOCIATED CONTENT

Supporting Information

The Supporting Information is available free of charge at XXXXX. Table S1. Nomenclature; Materials and Characterization (Tables S1-S5 and Figure S1); Conventional Mixed Ionic Electronic Conduction Theory (c-MIEC) (Figure S2); Thermodynamic Factor for Electrochemical Intercalation Hosts; Analysis using x-MIEC (Figures S3-S8); Literature Properties for Li-ion Materials (Table S6)

AUTHOR INFORMATION

Corresponding Author

Brian J. Ingram – Chemical Sciences and Engineering Division, Joint Center for Energy Storage Research, Argonne National Laboratory, Lemont, IL 60439, USA; orcid.org/0000-0002-5219-7517; Email: ingram@anl.gov

Authors

Ian D. Johnson – Chemical Sciences and Engineering Division, Joint Center for Energy Storage Research, Argonne National Laboratory, Lemont, IL 60439, USA; orcid.org/0000-0001-5491-9627.

Aashutosh Mistry – Chemical Sciences and Engineering Division, Joint Center for Energy Storage Research, Argonne National Laboratory, Lemont, IL 60439, USA; orcid.org/0000-0002-4359-4975

Liang Yin – X-ray Science Division, Joint Center for Energy Storage Research, Argonne National Laboratory, Lemont, IL 60439, USA; Present Address: Tianmu Lake Institute of Advanced Energy Storage Technologies, Liyang City, Jiangsu Province, China; orcid.org/0000-0001-5396-782X

Megan Murphy – Department of Chemistry, Joint Center for Energy Storage Research, University of Illinois at Chicago, Illinois 60607, USA

Mark Wolfman – Chemical Sciences and Engineering Division, Argonne National Laboratory, Lemont, IL 60439, USA; orcid.org/0000-0001-5746-2984

Timothy T. Fister – Chemical Sciences and Engineering Division, Joint Center for Energy Storage Research, Argonne National Laboratory, Lemont, IL 60439, USA; orcid.org/0000-0001-6539-6170

Saul H. Lapidus – X-ray Science Division, Joint Center for Energy Storage Research, Argonne National Laboratory, Lemont, IL 60439, USA; orcid.org/0000-0002-7486-4325

Jordi Cabana – Department of Chemistry, Joint Center for Energy Storage Research, University of Illinois at Chicago, Illinois 60607, USA; orcid.org/0000-0002-2353-5986

Venkat Srinivasan – Joint Center for Energy Storage Research, Argonne National Laboratory, Lemont, IL 60439, USA; orcid.org/0000-0002-1248-5952

Author Contributions

I.D.J. and A.M. contributed equally to this work.

Notes

The authors declare no compete financial interest.

ACKNOWLEDGMENTS

This work was entirely supported as part of the Joint Center for Energy Storage Research (JCESR), an Energy Innovation Hub funded by the US Department of Energy (DOE), Office of Science, Basic Energy Sciences (BES), under contract DE-AC02-05CH11231.

Use of the Advanced Photon Source (APS) was supported by the U.S. Department of Energy, Office of Science, under Contract No. DE-AC02-06CH11357.

This research used resources at the Nanoscale-Ordered Materials Diffractometer (NOMAD) instrument at the Spallation Neutron Source, a DOE Office of Science User Facility operated by the Oak Ridge National Laboratory.

I.D.J, A.M., V.S, and B.I. thank multiple researchers including Drs. Nitash Balsara, Yet-Ming Chiang, Dennis Dees, Linda Nazar, Gerbrand Ceder, Donald Siegel, Jeff Sakamoto, Robert Darling, Adam Matzger, Thomas Vaid, Hakim Iddir, Adam Tornheim, and Pallab Barai who have inspired us with stimulating questions and insightful discussions as we made progress on this work.

REFERENCES

(1) Trahey, L.; Brushett, F. R.; Balsara, N. P.; Ceder, G.; Cheng, L.; Chiang, Y.-M.; Hahn, N. T.; Ingram, B. J.; Minteer, S. D.; Moore, J. S.; Mueller, K. T.; Nazar, L. F.; Persson, K. A.; Siegel, D. J.; Xu, K.; Zavadil, K. R.; Srinivasan, V.; Crabtree, G. W. Energy Storage Emerging: A Perspective from the Joint Center for Energy Storage Research. *Proc. Natl. Acad. Sci. U.S.A.* **2020**, *117* (23), 12550–12557. DOI: 10.1073/pnas.1821672117.

(2) Canepa, P.; Sai Gautam, G.; Hannah, D. C.; Malik, R.; Liu, M.; Gallagher, K. G.; Persson, K. A.; Ceder, G. Odyssey of Multivalent Cathode Materials: Open Questions and Future Challenges. *Chem. Rev.* **2017**, *117* (5), 4287–4341. DOI: 10.1021/acs.chemrev.6b00614.

(3) Whittingham, M. S. Ultimate Limits to Intercalation Reactions for Lithium Batteries. *Chem. Rev.* **2014**, *114* (23), 11414–11443. DOI: 10.1021/cr5003003.

(4) Armand, M.; Tarascon, J.-M. Building Better Batteries. *Nature* **2008**, *451* (7179), 652–657. DOI: 10.1038/451652a.

(5) Ingram, B. J. CHAPTER 8 High Energy Density Insertion Cathode Materials. In *Magnesium Batteries: Research and Applications*; The Royal Society of Chemistry, 2019; pp 187–207. DOI: 10.1039/9781788016407-00187.

(6) Liu, M.; Rong, Z.; Malik, R.; Canepa, P.; Jain, A.; Ceder, G.; Persson, K. A. Spinel Compounds as Multivalent Battery Cathodes: A Systematic Evaluation Based on Ab Initio Calculations. *Energy Environ. Sci.* **2015**, *8* (3), 964–974. DOI: 10.1039/C4EE03389B.

(7) Bayliss, R. D.; Key, B.; Sai Gautam, G.; Canepa, P.; Kwon, B. J.; Lapidus, S. H.; Dogan, F.; Adil, A. A.; Lipton, A. S.; Baker, P. J.; Ceder, G.; Vaughey, J. T.; Cabana, J. Probing Mg Migration in Spinel Oxides. *Chem. Mater.* **2020**, *32* (2), 663–670. DOI: 10.1021/acs.chemmater.9b02450.

(8) Truong, Q. D.; Kobayashi, H.; Nayuki, K.; Sasaki, Y.; Honma, I. Atomic-Scale Observation of Phase Transition of MgMn2O4 Cubic Spinel upon the Charging in Mg-Ion Battery. *Solid State Ionics* **2020**, *344* (November 2019), 115136–115136. DOI: 10.1016/j.ssi.2019.115136.

(9) Knight, J. C.; Therese, S.; Manthiram, A. On the Utility of Spinel Oxide Hosts for Magnesium-Ion Batteries. *ACS Appl. Mater. Interfaces* **2015**, *7* (41), 22953–22961. DOI: 10.1021/acsami.5b06179.

(10) Hu, L.; Johnson, I. D.; Kim, S.; Nolis, G. M.; Freeland, J. W.; Yoo, H. D.; Fister, T. T.; McCafferty, L.; Ashton, T. E.; Darr, J. A.; Cabana, J. Tailoring the Electrochemical Activity of Magnesium Chromium Oxide towards Mg Batteries through Control of Size and Crystal Structure. *Nanoscale* **2019**, *11* (2), 639–646. DOI: 10.1039/C8NR08347A.

(11) Johnson, I. D.; Ingram, B. J.; Cabana, J. The Quest for Functional Oxide Cathodes for Magnesium Batteries: A Critical Perspective. *ACS Energy Lett.* **2021**, *6* (5), 1892–1900. DOI: 10.1021/acsenergylett.1c00416.

(12) Kwon, B. J.; Lau, K.-C.; Park, H.; Wu, Y. A.; Hawthorne, K. L.; Li, H.; Kim, S.; Bolotin, I. L.; Fister, T. T.; Zapol, P.; Klie, R. F.; Cabana, J.; Liao, C.; Lapidus, S. H.; Key, B.; Vaughey, J. T. Probing Electrochemical Mg-Ion Activity in $MgCr_{2-x}V_xO4$ Spinel Oxides. *Chem. Mater.* **2020**, *32* (3), 1162–1171. DOI: 10.1021/acs.chemmater.9b04206.

(13) Hu, L.; Jokisaari, J. R.; Kwon, B. J.; Yin, L.; Kim, S.; Park, H.; Lapidus, S. H.; Klie, R. F.; Key, B.; Zapol, P.; Ingram, B. J.; Vaughey, J. T.; Cabana, J. High Capacity for Mg^{2+} Deintercalation in Spinel Vanadium Oxide Nanocrystals. *ACS Energy Lett.* **2020**, *5* (8), 2721–2727. DOI: 10.1021/acsenergylett.0c01189.

(14) Yin, L.; Kwon, B. J.; Choi, Y.; Bartel, C. J.; Yang, M.; Liao, C.; Key, B.; Ceder, G.; Lapidus, S. H. Operando X-Ray Diffraction Studies of the Mg-Ion Migration Mechanisms in Spinel Cathodes for Rechargeable Mg-Ion Batteries. *J. Am. Chem. Soc.* **2021**, *143* (28), 10649–10658. DOI: 10.1021/jacs.1c04098.

(15) Kwon, B. J.; Yin, L.; Park, H.; Parajuli, P.; Kumar, K.; Kim, S.; Yang, M.; Murphy, M.; Zapol, P.; Liao, C.; Fister, T. T.; Klie, R. F.; Cabana, J.; Vaughey, J. T.; Lapidus, S. H.; Key, B. High Voltage Mg-Ion Battery Cathode via a Solid Solution Cr–Mn Spinel Oxide. *Chem. Mater.* **2020**, *32* (15), 6577–6587. DOI: 10.1021/acs.chemmater.0c01988.

(16) Okamoto, S.; Ichitsubo, T.; Kawaguchi, T.; Kumagai, Y.; Oba, F.; Yagi, S.; Shimokawa, K.; Goto, N.; Doi, T.; Matsubara, E. Intercalation and Push-Out Process with Spinel-to-Rocksalt Transition on Mg Insertion into Spinel Oxides in Magnesium Batteries. *Adv. Sci.* **2015**, *2* (8), 1500072. DOI: 10.1002/advs.201500072.

(17) Hatakeyama, T.; L. Okamoto, N.; Shimokawa, K.; Li, H.; Nakao, A.; Uchimoto, Y.; Tanimura, H.; Kawaguchi, T.; Ichitsubo, T. Electrochemical Phase Transformation Accompanied with Mg Extraction and Insertion in a Spinel $MgMn_2O_4$ Cathode Material. *Phys. Chem. Chem. Phys.* **2019**, *21* (42), 23749–23757. DOI: 10.1039/C9CP04461B.

(18) Johnson, I. D.; Nolis, G.; Yin, L.; Yoo, H. D.; Parajuli, P.; Mukherjee, A.; Andrews, J. L.; Lopez, M.; Klie, R. F.; Banerjee, S.; Ingram, B. J.; Lapidus, S.; Cabana, J.; Darr, J. A. Enhanced Charge Storage of Nanometric ζ-V_2O_5 in Mg Electrolytes. *Nanoscale* **2020**, *12* (43), 22150–22160. DOI: 10.1039/D0NR05060A.

(19) Sun, X.; Blanc, L.; Nolis, G. M.; Bonnick, P.; Cabana, J.; Nazar, L. F. NaV1.25Ti0.75O4: A Potential Post-Spinel Cathode Material for Mg Batteries. *Chem. Mater.* **2018**, *30* (1), 121–128. DOI: 10.1021/acs.chemmater.7b03383.

(20) Andrews, J. L.; Mukherjee, A.; Yoo, H. D.; Parija, A.; Marley, P. M.; Fakra, S.; Prendergast, D.; Cabana, J.; Klie, R. F.; Banerjee, S. Reversible Mg-Ion Insertion in a Metastable One-Dimensional Polymorph of V_2O_5. *Chem* **2018**, *4* (3), 564–585. DOI: 10.1016/j.chempr.2017.12.018.

(21) Yoo, H. D.; Jokisaari, J. R.; Yu, Y.-S.; Kwon, B. J.; Hu, L.; Kim, S.; Han, S.-D.; Lopez, M.; Lapidus, S. H.; Nolis, G. M.; Ingram, B. J.; Bolotin, I.; Ahmed, S.; Klie, R. F.; Vaughey, J. T.; Fister, T. T.; Cabana, J. Intercalation of Magnesium into a Layered Vanadium Oxide with High Capacity. *ACS Energy Lett.* **2019**, *4* (7), 1528–1534. DOI: 10.1021/acsenergylett.9b00788.

(22) Newman, J.; Tiedemann, W. Porous-Electrode Theory with Battery Applications. *AIChE Journal* **1975**, *21* (1), 25–41. DOI: 10.1002/aic.690210103.

(23) Doyle, M.; Fuller, T. F.; Newman, J. Modeling of Galvanostatic Charge and Discharge of the Lithium/Polymer/Insertion Cell. *J. Electrochem. Soc.* **1993**, *140* (6), 1526. DOI: 10.1149/1.2221597.

(24) Mistry, A. N.; Smith, K.; Mukherjee, P. P. Secondary-Phase Stochastics in Lithium-Ion Battery Electrodes. *ACS Appl. Mater. Interfaces* **2018**, *10* (7), 6317–6326. DOI: 10.1021/acsami.7b17771.

(25) Mistry, A.; Trask, S.; Dunlop, A.; Jeka, G.; Polzin, B.; Mukherjee, P. P.; Srinivasan, V. Quantifying Negative Effects of Carbon-Binder Networks from Electrochemical Performance of

Porous Li-Ion Electrodes. *J. Electrochem. Soc.* **2021**, *168* (7), 070536. DOI: 10.1149/1945-7111/ac1033.

(26) Mistry, A.; Usseglio-Viretta, F. L. E.; Colclasure, A.; Smith, K.; Mukherjee, P. P. Fingerprinting Redox Heterogeneity in Electrodes during Extreme Fast Charging. *J. Electrochem. Soc.* **2020**, *167* (9), 090542. DOI: 10.1149/1945-7111/ab8fd7.

(27) Forouzan, M. M.; Mazzeo, B. A.; Wheeler, D. R. Modeling the Effects of Electrode Microstructural Heterogeneities on Li-Ion Battery Performance and Lifetime. *J. Electrochem. Soc.* **2018**, *165* (10), A2127. DOI: 10.1149/2.1281809jes.

(28) Wu, S.-L.; Zhang, W.; Song, X.; Shukla, A. K.; Liu, G.; Battaglia, V.; Srinivasan, V. High Rate Capability of $Li(Ni_{1/3}Mn_{1/3}Co_{1/3})O_2$ Electrode for Li-Ion Batteries. *J. Electrochem. Soc.* **2012**, *159* (4), A438. DOI: 10.1149/2.062204jes.

(29) Amin, R.; Ravnsbæk, D. B.; Chiang, Y.-M. Characterization of Electronic and Ionic Transport in $Li_{1-x}Ni_{0.8}Co_{0.15}Al_{0.05}O_2$ (NCA). *J. Electrochem. Soc.* **2015**, *162* (7), A1163. DOI: 10.1149/2.0171507jes.

(30) Amin, R.; Chiang, Y.-M. Characterization of Electronic and Ionic Transport in $Li_{1-x}Ni_{0.33}Mn_{0.33}Co_{0.33}O_2$ (NMC333) and $Li_{1-x}Ni_{0.50}Mn_{0.20}Co_{0.30}O_2$ (NMC523) as a Function of Li Content. *J. Electrochem. Soc.* **2016**, *163* (8), A1512. DOI: 10.1149/2.0131608jes.

(31) Amin, R.; Maier, J.; Balaya, P.; Chen, D. P.; Lin, C. T. Ionic and Electronic Transport in Single Crystalline $LiFePO_4$ Grown by Optical Floating Zone Technique. *Solid State Ionics* **2008**, *179* (27), 1683–1687. DOI: 10.1016/j.ssi.2008.01.079.

(32) Verma, A.; Smith, K.; Santhanagopalan, S.; Abraham, D.; Yao, K. P.; Mukherjee, P. P. Galvanostatic Intermittent Titration and Performance Based Analysis of $LiNi_{0.5}Co_{0.2}Mn_{0.3}O_2$ Cathode. *J. Electrochem. Soc.* **2017**, *164* (13), A3380. DOI: 10.1149/2.1701713jes.

(33) Dees, D. W.; Kawauchi, S.; Abraham, D. P.; Prakash, J. Analysis of the Galvanostatic Intermittent Titration Technique (GITT) as Applied to a Lithium-Ion Porous Electrode. *J Power Sources* **2009**, *189* (1), 263–268. DOI: 10.1016/j.jpowsour.2008.09.045.

(34) Weppner, W.; Huggins, R. A. Determination of the Knetic Parameters of Mixed-Conducting Electrodes and Application of the System Li_3Sb. *J. Electrochem. Soc.* **1977**, *124* (10), 1569–1578.

(35) Landesfeind, J.; Hosaka, T.; Graf, M.; Kubota, K.; Komaba, S.; Gasteiger, H. A. Comparison of Ionic Transport Properties of Non-Aqueous Lithium and Sodium Hexafluorophosphate Electrolytes. *J. Electrochem. Soc.* **2021**, *168* (4), 040538. DOI: 10.1149/1945-7111/abf8d9.

(36) Landesfeind, J.; Gasteiger, H. A. Temperature and Concentration Dependence of the Ionic Transport Properties of Lithium-Ion Battery Electrolytes. *J. Electrochem. Soc.* **2019**, *166* (14), A3079. DOI: 10.1149/2.0571912jes.

(37) Wang, A. A.; Hou, T.; Karanjavala, M.; Monroe, C. W. Shifting-Reference Concentration Cells to Refine Composition-Dependent Transport Characterization of Binary Lithium-Ion Electrolytes. *Electrochimica Acta* **2020**, *358*, 136688. DOI: 10.1016/j.electacta.2020.136688.

(38) Hou, T.; Monroe, C. W. Composition-Dependent Thermodynamic and Mass-Transport Characterization of Lithium Hexafluorophosphate in Propylene Carbonate. *Electrochimica Acta* **2020**, *332*, 135085. DOI: 10.1016/j.electacta.2019.135085.

(39) Klett, M.; Giesecke, M.; Nyman, A.; Hallberg, F.; Lindström, R. W.; Lindbergh, G.; Furó, I. Quantifying Mass Transport during Polarization in a Li Ion Battery Electrolyte by in Situ 7Li NMR Imaging. *J. Am. Chem. Soc.* **2012**, *134* (36), 14654–14657. DOI: 10.1021/ja305461j.

(40) Lundgren, H.; Behm, M.; Lindbergh, G. Electrochemical Characterization and Temperature Dependency of Mass-Transport Properties of LiPF6 in EC:DEC. *J. Electrochem. Soc.* **2014**, *162* (3), A413. DOI: 10.1149/2.0641503jes.

(41) Valøen, L. O.; Reimers, J. N. Transport Properties of LiPF6-Based Li-Ion Battery Electrolytes. *J. Electrochem. Soc.* **2005**, *152* (5), A882. DOI: 10.1149/1.1872737.

(42) Liu, G.; Zheng, H.; Song, X.; Battaglia, V. S. Particles and Polymer Binder Interaction: A Controlling Factor in Lithium-Ion Electrode Performance. *J. Electrochem. Soc.* **2011**, *159* (3), A214. DOI: 10.1149/2.024203jes.

(43) Zheng, H.; Yang, R.; Liu, G.; Song, X.; Battaglia, V. S. Cooperation between Active Material, Polymeric Binder and Conductive Carbon Additive in Lithium Ion Battery Cathode. *J. Phys. Chem. C* **2012**, *116* (7), 4875–4882. DOI: 10.1021/jp208428w.

(44) Lanterman, B. J.; Riet, A. A.; Gates, N. S.; Flygare, J. D.; Cutler, A. D.; Vogel, J. E.; Wheeler, D. R.; Mazzeo, B. A. Micro-Four-Line Probe to Measure Electronic Conductivity and Contact Resistance of Thin-Film Battery Electrodes. *J. Electrochem. Soc.* **2015**, *162* (10), A2145. DOI: 10.1149/2.0581510jes.

(45) Lipson, A. L.; Han, S.-D.; Pan, B.; See, K. A.; Gewirth, A. A.; Liao, C.; Vaughey, J. T.; Ingram, B. J. Practical Stability Limits of Magnesium Electrolytes. *J. Electrochem. Soc.* **2016**, *163* (10), A2253–A2257. DOI: 10.1149/2.0451610jes.

(47) Hebb, M. H. Electrical Conductivity of Silver Sulfide. *J. Chem. Phys.* **1952**, *20* (1), 185–190. DOI: 10.1063/1.1700165.

(48) Wagner, C. Beitrag zur Theorie des Anlaufvorgangs. *Zeitschrift für Physikalische Chemie* **1933**, *21B* (1), 25–41. DOI: 10.1515/zpch-1933-2105.

(49) Yokota, I. On the Theory of Mixed Conduction with Special Reference to Conduction in Silver Sulfide Group Semiconductors. *J. Phys. Soc. Jpn.* **1961**, *16* (11), 2213–2223. DOI: 10.1143/JPSJ.16.2213.

(50) McLachlan, D. S.; Blaszkiewicz, M.; Newnham, R. E. Electrical Resistivity of Composites. *J. Electrochem. Soc.* **1990**, *73* (8), 2187–2203. DOI: 10.1111/j.1151-2916.1990.tb07576.x.

(51) Stefan, E.; Connor, P. A.; Azad, A. K.; Irvine, J. T. S. Structure and Properties of $MgM_xCr_{2-x}O_4$ (M = Li, Mg, Ti, Fe, Cu, Ga) Spinels for Electrode Supports in Solid Oxide Fuel Cells. *J. Mater. Chem. A* **2014**, *2* (42), 18106–18114. DOI: 10.1039/C4TA03633F.

(52) Yeh, T. C.; Perry, N. H.; Mason, T. O. Nanograin Composite Model Studies of Nanocrystalline Gadolinia-Doped Ceria. *J. Am. Ceram. Soc.* **2011**, *94* (4), 1073–1078. DOI: 10.1111/j.1551-2916.2010.04200.x.

(53) O'Neill, H. St. C.; Dollase, W. A. Crystal Structures and Cation Distributions in Simple Spinels from Powder XRD Structural Refinements: $MgCr_2O_4$, $ZnCr_2O_4$, Fe_3O_4 and the Temperature Dependence of the Cation Distribution in $ZnAl_2O_4$. *Phys Chem Minerals* **1994**, *20* (8), 541–555. DOI: 10.1007/BF00211850.

(54) Maier, J. Defect Chemistry and Conductivity Effects in Heterogeneous Solid Electrolytes. *J. Electrochem. Soc.* **1987**, *134* (6), 1524. DOI: 10.1149/1.2100703.

(55) Riess, I. Four Point Hebb-Wagner Polarization Method for Determining the Electronic Conductivity in Mixed Ionic-Electronic Conductors. *Solid State Ionics* **1992**, *51* (3), 219–229. DOI: 10.1016/0167-2738(92)90204-3.

(56) Irvine, J. T. S.; Sinclair, D. C.; West, A. R. Electroceramics: Characterization by Impedance Spectroscopy. *Adv. Mater.* **1990**, *2* (3), 132–138. DOI: 10.1002/adma.19900020304.

(57) Maier, J. Electrochemical Investigation Methods of Ionic Transport Properties in Solids. *Sol. St. Phen.* **1994**, *39–40*, 35–60. DOI: 10.4028/www.scientific.net/SSP.39-40.35.

(58) Lai, W.; Haile, S. M. Impedance Spectroscopy as a Tool for Chemical and Electrochemical Analysis of Mixed Conductors: A Case Study of Ceria. *J. Am. Ceram. Soc.* **2005**, *88* (11), 2979–2997. DOI: 10.1111/j.1551-2916.2005.00740.x.

(59) Maier, J. Ionics versus Electronics, and the General Case of Mixed Conductor. *Ann. Phys.* **2006**, *15* (7–8), 469–479. DOI: 10.1002/andp.200510201.

(60) Wang, M. J.; Wolfenstine, J. B.; Sakamoto, J. Mixed Electronic and Ionic Conduction Properties of Lithium Lanthanum Titanate. *Adv. Funct. Mater.* **2020**, *30* (10), 1909140. DOI: 10.1002/adfm.201909140.

(61) Tuller, H. L. Ionic Conduction in Nanocrystalline Materials. *Solid State Ionics* **2000**, *131* (1), 143–157. DOI: 10.1016/S0167-2738(00)00629-9.

(62) Kidner, N. J.; Homrighaus, Z. J.; Ingram, B. J.; Mason, T. O.; Garboczi, E. J. Impedance/Dielectric Spectroscopy of

Electroceramics - Part 2: Grain Shape Effects and Local Properties of Polycrystalline Ceramics. *J. Electroceram.* **2005**, *14* (3), 293–301. DOI: 10.1007/s10832-005-0968-1.

(63) Kidner, N. J.; Homrighaus, Z. J.; Ingram, B. J.; Mason, T. O.; Garboczi, E. J. Impedance/Dielectric Spectroscopy of Electroceramics - Part 1: Evaluation of Composite Models for Polycrystalline Ceramics. *J. Electroceram.* **2005**, *14* (3), 283–291. DOI: 10.1007/s10832-005-0969-0.

(64) Boukamp, B. A.; Bouwmeester, H. J. M. Interpretation of the Gerischer Impedance in Solid State Ionics. *Solid State Ionics* **2003**, *157* (1), 29–33. DOI: 10.1016/S0167-2738(02)00185-6.

(65) Stefan, E.; Irvine, J. T. S. Synthesis and Characterization of Chromium Spinels as Potential Electrode Support Materials for Intermediate Temperature Solid Oxide Fuel Cells. *J. Mater. Sci.* **2011**, *46* (22), 7191–7197. DOI: 10.1007/s10853-010-4489-1.

(66) Christensen, J.; Newman, J. A Mathematical Model of Stress Generation and Fracture in Lithium Manganese Oxide. *J. Electrochem. Soc.* **2006**, *153* (6), A1019. DOI: 10.1149/1.2185287.

(67) Christensen, J.; Newman, J. Stress Generation and Fracture in Lithium Insertion Materials. *J. Solid State Electrochem.* **2006**, *10* (5), 293–319. DOI: 10.1007/s10008-006-0095-1.

(68) Balsara, N. P.; Newman, J. Relationship between Steady-State Current in Symmetric Cells and Transference Number of Electrolytes Comprising Univalent and Multivalent Ions. *J. Electrochem. Soc.* **2015**, *162* (14), A2720. DOI: 10.1149/2.0651514jes.

(69) Meyers, J. P.; Doyle, M.; Darling, R. M.; Newman, J. The Impedance Response of a Porous Electrode Composed of Intercalation Particles. *J. Electrochem. Soc.* **2000**, *147* (8), 2930. DOI: 10.1149/1.1393627.

(70) Ferraro, M. E.; Trembacki, B. L.; Brunini, V. E.; Noble, D. R.; Roberts, S. A. Electrode Mesoscale as a Collection of Particles: Coupled Electrochemical and Mechanical Analysis of NMC Cathodes. *J. Electrochem. Soc.* **2020**, *167* (1), 013543. DOI: 10.1149/1945-7111/ab632b.

(71) Srinivasan, V.; Newman, J. Discharge Model for the Lithium Iron-Phosphate Electrode. *J. Electrochem. Soc.* **2004**, *151* (10), A1517. DOI: 10.1149/1.1785012.

(72) Liu, G.; Zheng, H.; Kim, S.; Deng, Y.; Minor, A. M.; Song, X.; Battaglia, V. S. Effects of Various Conductive Additive and Polymeric Binder Contents on the Performance of a Lithium-Ion Composite Cathode. *J. Electrochem. Soc.* **2008**, *155* (12), A887. DOI: 10.1149/1.2976031.

(73) Park, M.; Zhang, X.; Chung, M.; Less, G. B.; Sastry, A. M. A Review of Conduction Phenomena in Li-Ion Batteries. *J. Power Sources* **2010**, *195* (24), 7904–7929. DOI: 10.1016/j.jpowsour.2010.06.060.

(74) Dees, D. W.; Rodrigues, M.-T. F.; Kalaga, K.; Trask, S. E.; Shkrob, I. A.; Abraham, D. P.; Jansen, A. N. Apparent Increasing Lithium Diffusion Coefficient with Applied Current in Graphite. *J. Electrochem. Soc.* **2020**, *167* (12), 120528. DOI: 10.1149/1945-7111/abaf9f.

(75) Xia, H.; Lu, L.; Ceder, G. Li Diffusion in LiCoO2 Thin Films Prepared by Pulsed Laser Deposition. *J. Power Sources* **2006**, *159* (2), 1422–1427. DOI: 10.1016/j.jpowsour.2005.12.012.

(76) Mistry, A. N.; Grundy, L. S.; Halat, D.; Newman, J.; Balsara, N. P.; Srinivasan, V. Effect of Solvent Motion on Ion Transport in Electrolytes. *J. Electrochem. Soc.* **2022**, 169 (4), 040524. DOI: 10.1149/1945-7111/ac6329.

(77) Newman, J.; Bennion, D.; Tobias, C. W. Mass Transfer in Concentrated Binary Electrolytes. *Berichte der Bunsengesellschaft für physikalische Chemie* **1965**, *69* (7), 608–612. DOI: 10.1002/bbpc.19650690712.

(78) Newman, J.; Chapman, T. W. Restricted Diffusion in Binary Solutions. *AIChE J.* **1973**, *19* (2), 343–348. DOI: 10.1002/aic.690190220.

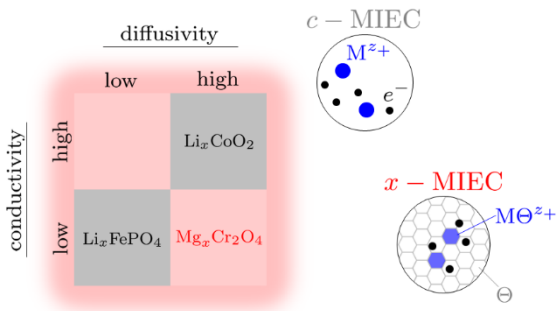
diffusivity
low
high
conductivity
high
low
Li_xCoO_2
Li_xFePO_4
$Mg_xCr_2O_4$
$c-$MIEC
M^{z+}
e^-
$x-$MIEC
$M\Theta^{z+}$
Θ